

Precision cosmology with time delay lenses: high resolution imaging requirements

Xiao-Lei Meng,¹ Tommaso Treu,^{1,2} Adriano Agnello,^{1,2} Matthew W. Auger,³ Kai Liao,^{1,2} Philip J. Marshall⁴

¹Department of Physics, University of California, Santa Barbara, CA 93106, USA

²Physics and Astronomy Building, 430 Portola Plaza, Box 951547, Los Angeles, CA 90095-1547, USA

³Institute of Astronomy, UK

⁴Kavli Institute for Particle Astrophysics and Cosmology, Stanford University, 452 Lomita Mall, Stanford, CA 94305, USA

E-mail: xlmeng919@gmail.com

Abstract. Lens time delays are a powerful probe of cosmology, provided that the gravitational potential of the main deflector can be modeled with sufficient precision. Recent work has shown that this can be achieved by detailed modeling of the host galaxies of lensed quasars. The distortion of the images as measured over large number of pixels provides tight constraints on the difference between the gravitational potential between the quasar image positions, and thus on cosmology in combination with the measured time delay. We carry out a systematic exploration of the high resolution imaging required to exploit the thousands of lensed quasars that will be discovered by current and upcoming surveys with the next decade. Specifically we simulate realistic lens systems as imaged by the Hubble Space Telescope (HST), James Webb Space Telescope (JWST), ground based adaptive optics images taken with Keck or the Thirty Meter Telescope (TMT). We compare the performance of these pointed observations with that of images taken by the Euclid-VIS, Wide-Field Infrared Survey Telescope (WFIRST) and Large Synoptic Survey Telescope (LSST) surveys. We use as our metric the precision with which the slope γ' of the total mass density profile $\rho_{tot} \propto r^{-\gamma'}$ for the main deflector can be measured. Ideally, we require that the statistical error on γ' be less than 0.02, thus being subdominant with respect to other sources of random and systematic uncertainties. We find that survey data will likely have sufficient depth and resolution to meet the target only for the brighter gravitational lens systems, comparable to those discovered by the SDSS survey. For fainter systems, that will be discovered by current and future surveys, targeted follow-up will be required. However, the exposure time per target will be of order a few minutes per system with upcoming facilities, such as JWST, the Keck Next Generation Adaptive Optics System, and TMT, thus making the follow-up of hundreds of systems a practical and efficient cosmological probe.

Contents

1	Introduction	1
2	Summary of simulated instrumental setups	3
3	The Lens Sample	4
3.1	Parameters of the Sample of Mock Lenses	4
4	Description of the inference process	5
4.1	Image generating progress	5
4.1.1	Light Model	6
4.1.2	Mass Model	6
4.1.3	Point-Source Model	7
4.1.4	PSF	7
4.1.5	Image Noise	7
5	Results	8
6	Summary	8

1 Introduction

In the past few years, gravitational time delays [?] have emerged as a powerful and cost effective cosmological probe. Studies based on blind analysis have shown that a single system consisting of multiple images of a background quasar (at redshift z_s) lensed by a foreground massive elliptical galaxy at redshift z_d can be used to measure the so-called time delay distance with an uncertainty of 6-7% [? ? ?]. The time delay distance $D_{\Delta t}$ gives a direct measurement of the Hubble constant and allows one to break some the main degeneracies in the interpretation of cosmic microwave background data, thus providing tight constraints on parameters such as curvature and dark energy equation of state [? ? ? ? ?]. The time delay distance measurement of H_0 is comparable in terms of information content to that obtained via the cosmic distance ladder [? ?], in that is based on absolute distances and completely independent on the properties of the universe at $z > z_s$. Importantly, time delay distances are independent of the local distance ladder and thus provide a crucial test of any potential systematic uncertainties. Furthermore, being independent, the cosmic distance ladder and time delay distance constraints on H_0 can be statistically combined for additional gains in precision.

From an observational point of view, the attainment of precise and accurate time delay measurements relies on a few important ingredients. First, monitoring of the lensed quasars is required to obtain time delays with a few percent uncertainties. Dedicated monitoring campaigns have shown that this precision is achievable with 1-2m class telescopes at present time [?], or in the radio [?]. In the future, the exploitation of larger samples of lenses will require monitoring campaigns on 2-4m telescopes [?], or the deployment of long term high-cadence monitoring surveys, like the LSST [?]. Second, the spectroscopic redshift of the source and deflector must be measured . For current samples, this is typically a relatively straightforward step, requiring short exposures on 4-10m class telescopes [? ?]. Third, the gravitational potential of the main deflector needs to be constrained by the data so that the uncertainty on its difference between the location of the images is also of order

3%. This goal can be achieved by studying the extended structure of the lensed quasar host galaxy, and the stellar kinematics of the deflector galaxy [? ? ? ? ?]. Fourth, the combined effects of the inhomogenous mass distribution along the line of sight need to be taken into account. Recent work has shown that the line of sight effects can be sufficiently characterized by measuring the properties of galaxies and weak lensing signal in the field of the main deflector, and comparing with simulated lines of sight (Suyu++10,++13,++14, Greene++13,Collet++13).

However, whereas current samples have been limited to a few lenses, current and onging surveys (add references to DES, PANSTARRS, HSC, ATLAS) will discover 100s of lenses. These large samples will be extremely powerful cosmographic probes [? ?], provided that sufficient follow-up data will be available [?]. In this paper we carry out a feasibility study for future time delay surveys, focusing on the high-resolution imaging requirements. Specifically, we aim to investigate whether sufficient information will be available from survey data, or whether dedicated follow-up will be necessary. If dedicated follow-up will be necessary, we aim to provide an estimate of the amount of time that will be required per system. The multi-pronged nature of time delay lens follow-up makes it natural to follow the approach of addressing each component of the follow-up independently. The monitoring and spectroscopic follow-up requirements are described, e.g., by [? ?].

In order to make the problem tractable and the results general, we need a single simple metric to evaluate the quality of imaging data. In short, we need to quantify our ability to measure how the deflection angle (i.e. the derivative of the lensing potential) varies between the images, and thus how the extended images of the quasar host galaxy are stretched across the image. In practice, our ability to constrain the differential magnification will depend on the resolution of the data as well as on the number of pixels where the source is detected (hereafter *informative pixels*).

We choose to adopt as our metric the slope γ' of the total mass density profile of the form $\rho_{\text{tot}} \propto r^{-\gamma'}$ as measured by fitting elliptical power law models to the data. This profile is the simplest one that provides a realistic description of galaxy scale lenses [?], and the uncertainty γ' has been shown to be approximately proportional to the uncertainty on the gravitational potential differences and thus the time delay distance [1, 2, 3]. Intuitively, γ' is directly related to the variations of the lensing potential. In fact, if $\gamma' = 2$ (the so-called isothermal profile) the deflection angle is constant across the image and therefore all the images will appear to have the same radial magnification. If the profile is steeper/shallower, radial magnification will vary across the image, thus giving rise to images of different widths.

Naturally, for a real measurement it is important to explore different profiles and the role of the choice of the profile in the uncertainties. However, our goal is to estimate minimal requirements on the data quality. If the data quality is insufficient to constrain γ' it will also be insufficient to constrain more flexible models. Likewise, systematic errors not considered in this paper, such as those arising from incomplete knowledge of the PSF, will only increase the error budget. Thus, in order to leave room for additional sources of uncertainty in the error budget, we set a rather stringent requirement of 0.02 uncertainty of γ' (corresponding approximately to 2% per system on time delay distance). In other words, our target corresponds to the requirement that the *statistical* error arising from the image quality be subdominant with respect to those arising from modeling uncertainties, time delays, and line of sight effects.

This paper is organized as follows. In Section 2, we summarize the characteristics of the telescopes and instruments simulated as part of this work. Then, in Section 3, we describe the properties of the simulated lenses. Next, in Section 4 we describe the procedure used to carry out the inference. Our results are presented in Section 5. Finally, we discuss and summarize our work in Section 6. Throughout this paper, all magnitudes are given in the AB system. Even though our findings are independent of any cosmology, we adopt a spatially flat Λ CDM cosmology with $\Omega_m = 0.3$, $\Omega_\Lambda = 0.7$,

and the Hubble constant $H_0 = 70 \text{ km s}^{-1} \text{ Mpc}^{-1}$ when calculating distances.

2 Summary of simulated instrumental setups

We aim to carry out a systematic exploration of imaging requirements given current and future facilities. For a given lens system, the instrumental setup drives our ability to constrain γ' in a number of ways. First, the signal-to-noise ratio depends on the exposure-time adopted, sky or background noise in a chosen band, and the instrumental readout noise. Second, the pixel-size and the point-spread function (PSF) properties determine how finely one can map the system being observed, hence how robustly the deflections on either side of the lens can be quantified.

Here we summarize the main properties of instruments that will be considered in our simulations. In an effort to balance completeness with feasibility, we consider a suite of instruments that include ground and space based telescopes, and cadenced surveys where the total exposure cannot be set arbitrarily. Some of the choices are representative of a class of telescopes/instruments, for example we expect the performance of Keck Adaptive Optics to be a useful guidance for adaptive optics systems on other 8-10m class telescopes, and that of the Thirty Meter Telescope to be a guidance for other planned 20-30m class telescopes.

Table 1 and figure 1 display the main properties of the telescopes that are needed when generating images of mock gravitational lenses, taken from the instrument websites. Figure 2 shows the typical PSF of each instrument. In order to facilitate comparisons between instruments and telescopes, whenever possible we selected the filter/band for each configuration that is closer to the I -band in the optical and the K' -band in the near infrared. A brief description of each setup follows.

1. The Advanced Camera for Surveys (ACS) is chosen as our reference optical imager on board the Hubble Space Telescope (HST). In the chosen F814W filter its performance is comparable to those of WFC3 (slightly higher sensitivity and coarser pixel size). For simplicity, we neglect charge transfer inefficiency effects, assuming that they are negligible or can be corrected to the desired level. The PSF is simulated using the Tiny Tim software (reference)
2. The Near Infrared Camera (NIRCAM) on board the James Webb Space Telescope (JWST) is chosen as the next space based imaging capability. We select the broad F200W filter, where the image quality is virtually diffraction limited.
3. The current and planned adaptive optics systems [hereafter LGSAO & NGAO 4, 5, respectively] at the W.M.Keck Observatory are chosen to represent current and upcoming AO performance on 8-10m class telescopes. We consider the current instrument NIRC2, although further gains might be possible with an instrument upgrade in conjunction with the AO system upgrade. We adopt the typical configuration used for studies of gravitational lens systems [?]: K' filter, MCDS readout mode, read number $N = 16$, and narrow camera mode. A real observed PSF is used for the current AO system. The simulated PSF and performance characteristics of NGAO have been kindly provided by the NGAO team.
4. The infrared imager and spectrograph IRIS [6] working behind adaptive optics on the thirty Meter Telescope is selected to represent the performance of the extremely large telescopes that will be operational in the next decade. TMT. IRIS is expected to be close to diffraction limited in the K' band. The simulated PSF and performance characteristics of TMT-IRIS have been obtained from the IRIS team, from the TMT ETC¹ and from the paper by Do et al. (2014) [7].

¹http://tmt.mtk.nao.ac.jp/ETC_readme.html

5. Euclid is a space survey telescope planned to be launched by the European Space Agency. Euclid has two instruments: a high-resolution visible imager, and a NIR imaging instrument. We study the performance of the high-resolution visible imager, the more suitable to detailed gravitational lensing work, with the standard survey parameters. The instrument properties are taken from Schweitzer et al. 2010 [8], Penny et al. 2013 [9] and Cropper et al. 2014 [10]. Since the PSF is proprietary to the Euclid team, we adopt for simplicity a Gaussian function with full width half maximum $0.^{\circ}18$.
6. We study the survey mode of the 2.4m WFIRST space mission, focusing on the HLS Imaging Survey in the F184W filter. The instrument/survey properties are based on WFIRST-Astrophysics Focused Telescope Assets Final Report (by the Science Definition Team (ADT) and WFIRST Project) and WFIRST Exposure Time Calculator ². Since the final PSF was not available at the time of this writing we adopt a Gaussian function with FWHM $0.15''$.
7. The Large Synoptic Survey Telescope is designed to imaging surveys in the optical bands (out to ~ 1 micron). The survey and instrument properties are taken from Ivezic et al. 2008 (REFERENCE) and the LSST Science Requirements Document ³. The PSF of LSST will vary over time. We adopt a Gaussian PSF with FWHM $0.7''$ as representative of the image quality of LSST in the i-band.

3 The Lens Sample

Here we introduce our sample, four groups of lens system with galaxies at redshift $z_s = 1.071$ and 2.77 being multiply imaged by massive lens galaxies lying at $z_d = 0.351$ and 0.783 .

We have chosen four prototypical systems for this exploration, characterized as **faint** or **bright** and **double** or **quad** depending on the photometry and image configuration. This set of four main choices covers regimes with different numbers of informative pixels, which depend on the S/N ratio and on the number of images produced by the lens.

To remain as realistic as possible, the mocks are based upon lenses in the Sloan Lens ACS Survey (SLACS; Bolton et al. 2006 [13]; Treu et al. 2006 [14]; Koopmans et al. 2006 [15]; Gavazzi et al. 2007 [16]; Bolton et al. 2008a [17]; Gavazzi et al. 2008 [18]; Bolton et al. 2008b [19]; Treu et al. 2009 [20]; Auger et al. 2009 [21]; Auger et al. 2010 [22]; Newton et al. 2011 [23]; Shu et al. 2015 [24]; Papers I-XII, respectively) and the Strong Lensing Legacy Survey (SL2S; More et al. 2012 [25]; Gavazzi et al. 2012 2012ApJ...761..170G; Ruff et al. 2011 [26]; Sonnenfeld et al. 2013 [27]; Sonnenfeld et al. 2013 [28]; Sonnenfeld et al. 2015 [29]; Papers I-V, respectively, except for the first citation) samples.

3.1 Parameters of the Sample of Mock Lenses

The structural parameters of the four systems are listed in Table 2. When not explicitly known from existing data, mock model parameters are assigned via plausibility arguments as specified below. The source and deflector of the *bright* lens system configurations are built along SLACS J0330-0020 as modelled by Bolton et al. 2008a (SLACS V, [17]), Auger et al. 2009 (SLACS IX, [21]), and Newton et al. 2011 (SLACS XI, [23]). For the *faint* lens system configuration, the source and deflector have parameters from the Sonnenfeld et al. 2013 (SL2S III, [27]) model of SL2S J135949+553550 and the discussion with Sonnenfeld. Source and deflector magnitudes in the *bright* case for I and V bands

²<http://wfirrst-web.ipac.caltech.edu/wfDepc/wfDepc.jsp?etc>

³<http://www.lsst.org/files/docs/SRD.pdf>

are from Newton et al. 2011 ([23]), for K band are estimated based on the other colors, and typical spectral energy distributions (i.e. an early-type galaxy for the deflector and a star forming galaxy for the source). Meanwhile, source magnitudes in the *faint* case are arbitrarily set to 25.0 in all bands.

Deflector magnitudes in the *faint* case are not directly available from the data, so they require some extrapolations. The value for I band is based on Sonnenfeld et al. 2013 (SL2S III, [27]), while for K and VIS bands are estimated according to their wavelength, assuming typical spectral energy distributions. Unknown magnitudes in *K* band are assigned from *H*-band ones via $K_{AB} = H_{AB}$. In addition, the effective (half-light) radius which are fitted in *bright* systems are evaluated in different bands for getting a precise estimate of the effective radius and its uncertainties. Differently, a unique effective radius is asserted across bandpasses for the *faint* systems. That means color gradient in photometric information is ignored for simplicity as this approximation does not affect the ability to recover the masss density profile in any significant way [27].

For both the faint and the bright systems, the source positions are assigned so as to map the source in either two or four images. This choice allows us to explore whether the number of images makes any substantial difference while keeping the other properties of the systems fixed.

In order to construct realistic systems for time delay measurements, we need to add point sources to represent the lensed quasars. As described in the next section this is done in the image plane, in order to gain computational precision and efficiency. The magnification at the location of the images is calculated by solving the lens equation using gravlens (add reference to Keeton's paper). The source plane magnitudes of the point sources are chosen to be somewhat brighter then the host galaxy, as it is typically the case for medium luminosity AGN [e.g., ?], and have realistic colors for AGN at the source redshifts. The adopted magnitudes are listed in Table ???. We note that the bright source configuration is too bright to be practical for TMT, given its sensitivity (the exposure time scales as D^{-4} , where D is the telescope diameter, for background limited point source exposures). Realistically, observations of such bright systems would be completely dominated by overheads related to target acquisition and will only be carried out in extremely rare circumstances. Therefore we do not simulate TMT observations for the bright systems. Even for the fainter system, we elected to make the source galaxies artificially fainter (K26) in order to avoid saturating the central pixels while imaging deep enough to get a good enough signal to noise ratio on the host galaxy. As will be shown below the exposure time requirements for TMT are extremely short even in these cases.

4 Description of the inference process

In this section, we briefly present the progress of modeling the mock lens systems using defined models. By comparing the distribution of the ratio between the inferred values and the input, we obtain the desired estimate of the statistical precision with which each parameter can be determined. As motivated in the introduction, we are interested primarily in the mass density profile slope γ' . Therefore we will only show the statistics for that parameter, even though all the parameters are varied simultaneously during the inference. We first

4.1 Image generating progress

Before we fit the mock lens system we need to define the models to describe the source galaxy light, the lens galaxy light, and the lens mass. We start with the surface brightness distribution of the galaxies. To remap the source image onto the source plane, the mass model for the lens mass distribution is needed to build to represent the deflection angle. Similarly, we also need a model for the light distribution of the lens galaxy. A PSF is used to convolve the light of lens galaxy, lensed source galaxy and point-source. Furthermore, we introduce three terms to describe the noise adding

to the image, including counts noise, readout noise, and background noise. As described above, we will make a detailed description of surface brightness light model, lens model, point-source model, PSF, and instrument noise information in this subsection.

4.1.1 Light Model

We use Sérsic profile (Sérsic 1963 [30]; 1968 [31]) which is created to represent how the intensity I of a galaxy varies with distance R from its center to describe the light distributions of source and lens galaxies,

$$I(R) = I_e \exp \left[-k \left(\left(\frac{R}{R_{\text{eff}}} \right)^{\frac{1}{n}} - 1 \right) \right], \quad (4.1)$$

$$R(x, y, q) = \sqrt{qx^2 + y^2/q}, \quad (4.2)$$

(see Caon et al. 1993 [32]). The amplitude I_e is the intensity at the effective R_{eff} , the constant k is usually determined based on R_{eff} is the radius at which the major axis contains half of the total flux, the parameter n is named Sérsic index which is used to control the degree of the curvature of the radial light profile, the $\{x, y\}$ represents the galaxy positions, and q denotes the axis ratio.

An additional explanation is necessary here: the best-fit value of n correlates with galaxy size and luminosity. Most galaxies are fitted by Sérsic index in the range $0.6 \leq n \leq 10.0$ (Merritt et al. 2006 [33]). More centrally concentrated profile matches larger value of Sérsic index. For example, for giant elliptical galaxies, $n = 4$ is a good description.

4.1.2 Mass Model

Here we describe the distribution of the surface mass density for the lens galaxy. The deflector's mass profile is assigned within a class of power-law models,

$$\Sigma(x, y) = \Sigma_0(qX^2 + q^{-1}Y^2)^{-\gamma'}, \quad (4.3)$$

where q is the axis ratio, γ' represents the radial power-law slope, the $\{X, Y\}$ axes are rotated by some position angle w.r.to the canonical x (increasing to the West) and y (increasing to the North). This means that the $\{X, Y\}$ deflections scale as ..., where $g(\theta)$ a just function of the relative angle west-of-north. Fast methods to compute deflections from power-law profiles have been given by Barkana 1998 [34]. Power-law models of elliptical galaxies (Evans 1994 [35]) have often been used with success over the years to model gravitational lenses. In utter generality, the lensing deflections are given by

$$\alpha(\theta) = \frac{2}{\theta} \int_0^\theta \theta d\theta \Sigma(\theta)/\Sigma_{\text{cr}} \quad (4.4)$$

where θ is the position angle, and

$$\Sigma_{\text{cr}} = \frac{c^2 D_s}{4\pi G D_d D_{ds}} \quad (4.5)$$

encompasses the relative positions of source, deflector and observer (the angular diameter to the deflector (D_d), to the source (D_s), and between the deflector and the source (D_{ds})). Then, in our power-law case the deflections can be rewritten conveniently as

$$\alpha(\vartheta) = \theta_E \left(\frac{\theta_E}{\vartheta} \right)^{\gamma'-2}, \quad (4.6)$$

$$(4.7)$$

where $\vartheta = R/D_d$, and R is the two-dimensional projected radius. θ_E here is the Einstein radius R_E , which is such that in the spherical case ($q = 1$) the mean dimensionless density $\langle \Sigma \rangle / \Sigma_{cr}$ within a circle of radius R_E is exactly 1. This is also the radius of a ring traced by the host of the quasar when this is exactly aligned with the lens galaxy.

Lensed image profiles are obtained by Inverse Ray Shooting:.. First, each pixel position in the image plane is mapped back to the source plane via the deflections in eq ... Then, we exploit the fact that surface-brightness is preserved by lensing, i.e.

$$\dots \quad (4.8)$$

In general, when dealing with more complex caustics from substructure **Vegetti** (????) or microlensing **Mediavilla** (????), rays are shot through an adaptive, triangular tessellation in the image place. Here, we can simply use a rectangular grid in the image-plane to obtain sufficiently accurate results.

4.1.3 Point-Source Model

4.1.4 PSF

For modeling the light of the lens galaxies, the lensed background galaxies and the lensed point sources, we use simulated PSFs for every instrument except for LGSAO. On the other hand, for Euclid, WFIRST, and LSST, Gaussian PSFs are adopted to generate mock data in this work by lack of sufficient information. The typical full width at half maximum (FWHM) of PSF with selected filter are 0.18, 0.15, and 0.7 respectively.

4.1.5 Image Noise

As mentioned above, clean lens system image can be created if light, mass and PSF model are defined precisely. However, noise also contributes pixel counts in a given exposure time except for the signals from lensed galaxy, deflector and point-source. To derive the noise in each pixel, there are three principle ingredients, include counts noise from the clean image, background noise depends on the instrument and wavelength, and readout noise based on instrument. The variance of total noise is given by

$$\text{Var}_{\text{noise}} = \sqrt{Ct + (B_{\text{sky}} + B_{\text{det}})tN_{\text{pix}} + N_{\text{read}}R^2N_{\text{pix}}} \quad (4.9)$$

where C is the signal from clean lens system in electrons per second from the CCD, t is the integration time in seconds, B_{sky} is the sky background in electrons per second per pixel, B_{det} is the detector dark current in electrons per second per pixel, N_{pix} is the total number of detector pixels which are integrated over to achieve C , N_{read} is the number of CCD readouts, and R is the read noise in electrons.

Normally, comparing with B_{sky} , the value of detector's dark current is negligibly small, so in this case we will only consider the former. For the high precision in observation, sufficiently long integrations should be given so that the CCD readout noise is not important. It should be note that as a consequence of atmospheric disturbance, the background noise in ground-based telescopes have greatly exceeded that in space telescopes.

The same code is used to generate the mock models and to fit them. The model fits the following parameters: **which ones?** Goodness of fit is assessed through the image-plane χ^2 , comparing the model and mock data surface brightness profiles. The quasar images are not used in the fit, which is performed just on the lensed host. This is because in reality, even in the absence of substructure lensing, the relative fluxes of the point-like images of the quasar can be appreciably affected by microlensing or dust lanes in the foreground. Uncertainties are obtained via MCMC exploration of the likelihood, which in this case is simply given by $\mathcal{L} \propto \exp[-\chi^2/2]$.

We reconstruct the galaxy's position, effective radii, axis ratio, position angle, and mass power law slope for the lens galaxy light and source light.

Here we describe how the mock lens models are generated, using power-law lenses. The deflectors mass profile is assigned within a class of power-law models,

We fix the source morphology parameters (position angle, inclination, ... and Sérsic index) to therefore, each QSO image have three parameters: position x,y ..., and amplitude.
is well described by the power-law...

Here we describe how the mock lens models are generated, using power-law lenses. The reader familiar with this topic can easily skip to the next Section.

The deflector's mass profile is assigned within a class of power-law models,

5 Results

Using the method described in Section..., we generate 30 simulations for each...

6 Summary

Acknowledgments

References

- [1] C. S. Kochanek, *What Do Gravitational Lens Time Delays Measure?*, *Astrophys. J.* **578** (Oct., 2002) 25–32, [[astro-ph/0205319](#)].
- [2] O. Wucknitz, *Degeneracies and scaling relations in general power-law models for gravitational lenses*, *Mon. Not. R. Astron. Soc.* **332** (June, 2002) 951–961, [[astro-ph/0202376](#)].
- [3] S. H. Suyu, *Cosmography from two-image lens systems: overcoming the lens profile slope degeneracy*, *Mon. Not. R. Astron. Soc.* **426** (Oct., 2012) 868–879, [[arXiv:1202.0287](#)].
- [4] P. L. Wizinowich, D. Le Mignant, A. H. Bouchez, R. D. Campbell, J. C. Y. Chin, A. R. Contos, M. A. van Dam, S. K. Hartman, E. M. Johansson, R. E. Lafon, H. Lewis, P. J. Stomski, D. M. Summers, C. G. Brown, P. M. Danforth, C. E. Max, and D. M. Pennington, *The W. M. Keck Observatory Laser Guide Star Adaptive Optics System: Overview*, *PASP* **118** (Feb., 2006) 297–309.
- [5] P. Wizinowich, S. Adkins, R. Dekany, D. Gavel, C. Max, R. Bartos, J. Bell, A. Bouchez, J. Chin, A. Conrad, A. Delacroix, E. Johansson, R. Kupke, C. Lockwood, J. Lyke, F. Marchis, E. McGrath, D. Medeiros, M. Morris, D. Morrison, C. Neyman, S. Panteleev, M. Pollard, M. Reinig, T. Stalcup, S. Thomas, M. Troy, K. Tsubota, V. Velur, K. Wallace, and E. Wetherell, *W. M. Keck Observatory's next-generation adaptive optics facility*, in *Society of Photo-Optical Instrumentation Engineers (SPIE) Conference Series*, vol. 7736 of *Society of Photo-Optical Instrumentation Engineers (SPIE) Conference Series*, p. 0, July, 2010.
- [6] J. E. Larkin, A. M. Moore, E. J. Barton, B. Bauman, K. Bui, J. Canfield, D. Crampton, A. Delacroix, M. Fletcher, D. Hale, D. Loop, C. Niehaus, A. C. Phillips, V. Reshetov, L. Simard, R. Smith, R. Suzuki, T. Usuda, and S. A. Wright, *The infrared imaging spectrograph (IRIS) for TMT: instrument overview*, in *Society of Photo-Optical Instrumentation Engineers (SPIE) Conference Series*, vol. 7735 of *Society of Photo-Optical Instrumentation Engineers (SPIE) Conference Series*, p. 29, July, 2010. [arXiv:1007.1973](#).
- [7] T. Do, S. A. Wright, A. J. Barth, E. J. Barton, L. Simard, J. E. Larkin, A. M. Moore, L. Wang, and B. Ellerbroek, *Prospects for Measuring Supermassive Black Hole Masses with Future Extremely Large Telescopes*, *Astron. J.* **147** (Apr., 2014) 93, [[arXiv:1401.7988](#)].

- [8] M. Schweitzer, R. Bender, R. Katterloher, F. Eisenhauer, R. Hofmann, R. Saglia, R. Holmes, O. Krause, H.-W. Rix, J. Booth, P. Fagrelius, J. Rhodes, S. Seshadri, A. Refregier, J. Amiaux, J.-L. Augueres, O. Boulade, C. Cara, A. Amara, S. Lilly, E. Atad-Ettedgui, A.-M. di Giorgio, L. Duvet, C. Kuehl, and M. Syed, *NIP: the near infrared imaging photometer for Euclid*, in *Society of Photo-Optical Instrumentation Engineers (SPIE) Conference Series*, vol. 7731 of *Society of Photo-Optical Instrumentation Engineers (SPIE) Conference Series*, p. 1, July, 2010.
- [9] M. T. Penny, E. Kerins, N. Rattenbury, J.-P. Beaulieu, A. C. Robin, S. Mao, V. Batista, S. Calchi Novati, A. Cassan, P. Fouqué, I. McDonald, J. B. Marquette, P. Tisserand, and M. R. Zapatero Osorio, *ExELS: an exoplanet legacy science proposal for the ESA Euclid mission - I. Cold exoplanets*, Mon. Not. R. Astron. Soc. **434** (Sept., 2013) 2–22, [[arXiv:1206.5296](#)].
- [10] M. Cropper, S. Pottinger, S.-M. Niemi, J. Denniston, R. Cole, M. Szafraniec, Y. Mellier, M. Berthé, J. Martignac, C. Cara, A. M. di Giorgio, A. Sciortino, S. Paltani, L. Genolet, J.-J. Fourmand, M. Charra, P. Guttridge, B. Winter, J. Endicott, A. Holland, J. Gow, N. Murray, D. Hall, J. Amiaux, R. Laureijs, G. Racca, J.-C. Salvignol, A. Short, J. Lorenzo Alvarez, T. Kitching, H. Hoekstra, and R. Massey, *VIS: the visible imager for Euclid*, in *Society of Photo-Optical Instrumentation Engineers (SPIE) Conference Series*, vol. 9143 of *Society of Photo-Optical Instrumentation Engineers (SPIE) Conference Series*, p. 0, Aug., 2014.
- [11] J. Green, P. Schechter, C. Baltay, R. Bean, D. Bennett, R. Brown, C. Conselice, M. Donahue, X. Fan, B. S. Gaudi, C. Hirata, J. Kalirai, T. Lauer, B. Nichol, N. Padmanabhan, S. Perlmutter, B. Rauscher, J. Rhodes, T. Roellig, D. Stern, T. Sumi, A. Tanner, Y. Wang, D. Weinberg, E. Wright, N. Gehrels, R. Sambruna, W. Traub, J. Anderson, K. Cook, P. Garnavich, L. Hillenbrand, Z. Ivezić, E. Kerins, J. Lunine, P. McDonald, M. Penny, M. Phillips, G. Rieke, A. Riess, R. van der Marel, R. K. Barry, E. Cheng, D. Content, R. Cutri, R. Goullioud, K. Grady, G. Helou, C. Jackson, J. Kruk, M. Melton, C. Peddie, N. Rioux, and M. Seiffert, *Wide-Field InfraRed Survey Telescope (WFIRST) Final Report*, ArXiv e-prints (Aug., 2012) [[arXiv:1208.4012](#)].
- [12] Z. Ivezić, J. A. Tyson, B. Abel, E. Acosta, R. Allsman, Y. AlSayyad, S. F. Anderson, J. Andrew, R. Angel, G. Angeli, R. Ansari, P. Antilogus, K. T. Arndt, P. Astier, E. Aubourg, T. Axelrod, D. J. Bard, J. D. Barr, A. Barrau, J. G. Bartlett, B. J. Bauman, S. Beaumont, A. C. Becker, J. Becla, C. Beldica, S. Bellavia, G. Blanc, R. D. Blandford, J. S. Bloom, J. Bogart, K. Borne, J. F. Bosch, D. Boutigny, W. N. Brandt, M. E. Brown, J. S. Bullock, P. Burchat, D. L. Burke, G. Cagnoli, D. Calabrese, S. Chandrasekharan, S. Chesley, E. C. Cheu, J. Chiang, C. F. Claver, A. J. Connolly, K. H. Cook, A. Cooray, K. R. Covey, C. Cribbs, W. Cui, R. Cutri, G. Daubard, G. Daues, F. Delgado, S. Digel, P. Doherty, R. Dubois, G. P. Dubois-Felsmann, J. Durech, M. Eracleous, H. Ferguson, J. Frank, M. Freemon, E. Gangler, E. Gawiser, J. C. Geary, P. Gee, M. Geha, R. R. Gibson, D. K. Gilmore, T. Glanzman, I. Goodenow, W. J. Gressler, P. Gris, A. Guyonnet, P. A. Hascall, J. Haupt, F. Hernandez, C. Hogan, D. Huang, M. E. Huffer, W. R. Innes, S. H. Jacoby, B. Jain, J. Jee, J. G. Jernigan, D. Jevremovic, K. Johns, R. L. Jones, C. Juramy-Gilles, M. Juric, S. M. Kahn, J. S. Kalirai, N. Kallivayalil, B. Kalmbach, J. P. Kantor, M. M. Kasliwal, R. Kessler, D. Kirkby, L. Knox, I. Kotov, V. L. Krabbendam, S. Krughoff, P. Kubanek, J. Kuczewski, S. Kulkarni, R. Lambert, L. Le Guillou, D. Levine, M. Liang, K. Lim, C. Lintott, R. H. Lupton, A. Mahabal, P. Marshall, S. Marshall, M. May, R. McKercher, M. Migliore, M. Miller, D. J. Mills, D. G. Monet, M. Moniez, D. R. Neill, J. Nieff, A. Nomerotski, M. Nordby, P. O'Connor, J. Oliver, S. S. Olivier, K. Olsen, S. Ortiz, R. E. Owen, R. Pain, J. R. Peterson, C. E. Petry, F. Pierfederici, S. Pietrowicz, R. Pike, P. A. Pinto, R. Plante, S. Plate, P. A. Price, M. Prouza, V. Radeka, J. Rajagopal, A. Rasmussen, N. Regnault, S. T. Ridgway, S. Ritz, W. Rosing, C. Roucelle, M. R. Rumore, S. Russo, A. Saha, B. Sassolas, T. L. Schalk, R. H. Schindler, D. P. Schneider, G. Schumacher, J. Sebag, G. H. Sembroski, L. G. Seppala, I. Shipsey, N. Silvestri, J. A. Smith, R. C. Smith, M. A. Strauss, C. W. Stubbs, D. Sweeney, A. Szalay, P. Takacs, J. J. Thaler, R. Van Berg, D. Vanden Berk, K. Vetter, F. Virieux, B. Xin, L. Walkowicz, C. W. Walter, D. L. Wang, M. Warner, B. Willman, D. Wittman, S. C. Wolff, W. M. Wood-Vasey, P. Yoachim, H. Zhan, and for the LSST Collaboration, *LSST: from Science Drivers to Reference Design and Anticipated Data Products*, ArXiv e-prints (May, 2008) [[arXiv:0805.2366](#)].

- [13] A. S. Bolton, S. Burles, L. V. E. Koopmans, T. Treu, and L. A. Moustakas, *The Sloan Lens ACS Survey. I. A Large Spectroscopically Selected Sample of Massive Early-Type Lens Galaxies*, *Astrophys. J.* **638** (Feb., 2006) 703–724, [[astro-ph/0511453](#)].
- [14] T. Treu, L. V. Koopmans, A. S. Bolton, S. Burles, and L. A. Moustakas, *The Sloan Lens ACS Survey. II. Stellar Populations and Internal Structure of Early-Type Lens Galaxies*, *Astrophys. J.* **640** (Apr., 2006) 662–672, [[astro-ph/0512044](#)].
- [15] L. V. E. Koopmans, T. Treu, A. S. Bolton, S. Burles, and L. A. Moustakas, *The Sloan Lens ACS Survey. III. The Structure and Formation of Early-Type Galaxies and Their Evolution since $z \sim 1$* , *Astrophys. J.* **649** (Oct., 2006) 599–615, [[astro-ph/0601628](#)].
- [16] R. Gavazzi, T. Treu, J. D. Rhodes, L. V. E. Koopmans, A. S. Bolton, S. Burles, R. J. Massey, and L. A. Moustakas, *The Sloan Lens ACS Survey. IV. The Mass Density Profile of Early-Type Galaxies out to 100 Effective Radii*, *Astrophys. J.* **667** (Sept., 2007) 176–190, [[astro-ph/0701589](#)].
- [17] A. S. Bolton, S. Burles, L. V. E. Koopmans, T. Treu, R. Gavazzi, L. A. Moustakas, R. Wayth, and D. J. Schlegel, *The Sloan Lens ACS Survey. V. The Full ACS Strong-Lens Sample*, *Astrophys. J.* **682** (Aug., 2008) 964–984, [[arXiv:0805.1931](#)].
- [18] R. Gavazzi, T. Treu, L. V. E. Koopmans, A. S. Bolton, L. A. Moustakas, S. Burles, and P. J. Marshall, *The Sloan Lens ACS Survey. VI. Discovery and Analysis of a Double Einstein Ring*, *Astrophys. J.* **677** (Apr., 2008) 1046–1059, [[arXiv:0801.1555](#)].
- [19] A. S. Bolton, T. Treu, L. V. E. Koopmans, R. Gavazzi, L. A. Moustakas, S. Burles, D. J. Schlegel, and R. Wayth, *The Sloan Lens ACS Survey. VII. Elliptical Galaxy Scaling Laws from Direct Observational Mass Measurements*, *Astrophys. J.* **684** (Sept., 2008) 248–259, [[arXiv:0805.1932](#)].
- [20] T. Treu, R. Gavazzi, A. Gorecki, P. J. Marshall, L. V. E. Koopmans, A. S. Bolton, L. A. Moustakas, and S. Burles, *The SLACS Survey. VIII. The Relation between Environment and Internal Structure of Early-Type Galaxies*, *Astrophys. J.* **690** (Jan., 2009) 670–682, [[arXiv:0806.1056](#)].
- [21] M. W. Auger, T. Treu, A. S. Bolton, R. Gavazzi, L. V. E. Koopmans, P. J. Marshall, K. Bundy, and L. A. Moustakas, *The Sloan Lens ACS Survey. IX. Colors, Lensing, and Stellar Masses of Early-Type Galaxies*, *Astrophys. J.* **705** (Nov., 2009) 1099–1115, [[arXiv:0911.2471](#)].
- [22] M. W. Auger, T. Treu, A. S. Bolton, R. Gavazzi, L. V. E. Koopmans, P. J. Marshall, L. A. Moustakas, and S. Burles, *The Sloan Lens ACS Survey. X. Stellar, Dynamical, and Total Mass Correlations of Massive Early-type Galaxies*, *Astrophys. J.* **724** (Nov., 2010) 511–525, [[arXiv:1007.2880](#)].
- [23] E. R. Newton, P. J. Marshall, T. Treu, M. W. Auger, R. Gavazzi, A. S. Bolton, L. V. E. Koopmans, and L. A. Moustakas, *The Sloan Lens ACS Survey. XI. Beyond Hubble Resolution: Size, Luminosity, and Stellar Mass of Compact Lensed Galaxies at Intermediate Redshift*, *Astrophys. J.* **734** (June, 2011) 104, [[arXiv:1104.2608](#)].
- [24] Y. Shu, A. S. Bolton, J. R. Brownstein, A. D. Montero-Dorta, L. V. E. Koopmans, T. Treu, R. Gavazzi, M. W. Auger, O. Czoske, P. J. Marshall, and L. A. Moustakas, *The Sloan Lens ACS Survey. XII. Extending Strong Lensing to Lower Masses*, *ArXiv e-prints* (July, 2014) [[arXiv:1407.2240](#)].
- [25] A. More, R. Cabanac, S. More, C. Alard, M. Limousin, J.-P. Kneib, R. Gavazzi, and V. Motta, *The CFHTLS-Strong Lensing Legacy Survey (SL2S): Investigating the Group-scale Lenses with the SARCS Sample*, *Astrophys. J.* **749** (Apr., 2012) 38, [[arXiv:1109.1821](#)].
- [26] A. J. Ruff, R. Gavazzi, P. J. Marshall, T. Treu, M. W. Auger, and F. Brault, *The SL2S Galaxy-scale Lens Sample. II. Cosmic Evolution of Dark and Luminous Mass in Early-type Galaxies*, *Astrophys. J.* **727** (Feb., 2011) 96, [[arXiv:1008.3167](#)].
- [27] A. Sonnenfeld, R. Gavazzi, S. H. Suyu, T. Treu, and P. J. Marshall, *The SL2S Galaxy-scale Lens Sample. III. Lens Models, Surface Photometry, and Stellar Masses for the Final Sample*, *Astrophys. J.* **777** (Nov., 2013) 97, [[arXiv:1307.4764](#)].

- [28] A. Sonnenfeld, T. Treu, R. Gavazzi, S. H. Suyu, P. J. Marshall, M. W. Auger, and C. Nipoti, *The SL2S Galaxy-scale Lens Sample. IV. The Dependence of the Total Mass Density Profile of Early-type Galaxies on Redshift, Stellar Mass, and Size*, *Astrophys. J.* **777** (Nov., 2013) 98, [[arXiv:1307.4759](https://arxiv.org/abs/1307.4759)].
- [29] A. Sonnenfeld, T. Treu, P. J. Marshall, S. H. Suyu, R. Gavazzi, M. W. Auger, and C. Nipoti, *The SL2S Galaxy-scale Lens Sample. V. Dark Matter Halos and Stellar IMF of Massive Early-type Galaxies Out to Redshift 0.8*, *Astrophys. J.* **800** (Feb., 2015) 94, [[arXiv:1410.1881](https://arxiv.org/abs/1410.1881)].
- [30] J. L. Sérsic, *Influence of the atmospheric and instrumental dispersion on the brightness distribution in a galaxy*, *Boletin de la Asociacion Argentina de Astronomia La Plata Argentina* **6** (1963) 41.
- [31] J. L. Sérsic, *Atlas de galaxias australes*. 1968.
- [32] N. Caon, M. Capaccioli, and M. D’Onofrio, *On the Shape of the Light Profiles of Early Type Galaxies*, *Mon. Not. R. Astron. Soc.* **265** (Dec., 1993) 1013, [[astro-ph/9309013](https://arxiv.org/abs/astro-ph/9309013)].
- [33] D. Merritt, A. W. Graham, B. Moore, J. Diemand, and B. Terzić, *Empirical Models for Dark Matter Halos. I. Nonparametric Construction of Density Profiles and Comparison with Parametric Models*, *Astron. J.* **132** (Dec., 2006) 2685–2700, [[astro-ph/0509417](https://arxiv.org/abs/astro-ph/0509417)].
- [34] R. Barkana, *Fast Calculation of a Family of Elliptical Mass Gravitational Lens Models*, *Astrophys. J.* **502** (Aug., 1998) 531–537, [[astro-ph/9802002](https://arxiv.org/abs/astro-ph/9802002)].
- [35] N. W. Evans, *The power-law galaxies*, *Mon. Not. R. Astron. Soc.* **267** (Mar., 1994) 333–360.

Table 1. Telescope and Instrument Properties

Telescope	Instrument	Filter	Zero Point	Readout Noise (e ⁻ /pixel)	Background Noise (e ⁻ /pixel/s)	Pixel Size (arcsec)
HST	ACS	F814W	25.94	4.20	0.11	0.050
JWST	NIRCAM	F200W	27.85	9.00	0.20	0.032
LGSАО	NIRC2	<i>K'</i>	28.04	5.75	26	0.010
NGAO	NIRC2	<i>K'</i>	28.04	5.75	26	0.010
TMT	IRIS	<i>K'</i>	31.10	2.00	21	0.004
Euclid	VIS	<i>r + i + z</i>	25.58	4.50	0.43	0.100
WFIRST	DRM(?)	F184	26.18	5.00	0.11	0.110
LSST	—	<i>I</i>	28.35	5.00	68	0.200

Observational facilities (telescopes and instruments) considered in this work. Zero points are given in the ABmag system. The VIS imager of Euclid spans the whole *r + i + z* wavelength range. The Keck 10-m telescope is considered both with the current (LGSАО) and next-generation (NGAO) adaptive optics capabilities.

Table 2. Surface Brightness Profile Models

Lens Name	R_{eff} (arcsec)	q	P.A. (deg)	n	Δx (arcsec)	Δy (arcsec)	m_I	m_K	m_{VIS}	m_H
Parameters for the source										
fainter system ^a	0.23	0.92	54.0	4.0	0.0662	-0.167	25.0	25.0	25.0	25.0
fainter system ^b	0.23	0.92	54.0	4.0	0.008	0.298	25.0	25.0	25.0	25.0
brighter system ^b	0.12	0.77	120.0	1.33	-0.195	0.34	22.73	22.0	23.46	22.0
brighter system ^a	0.12	0.77	120.0	1.33	0.01	-0.005	22.73	22.0	23.46	22.0
Parameters for the deflector										
fainter system	1.76	0.61	-9.6	4.0	—	—	20.69	19.7	21.13	19.7
brighter system	0.91	0.81	113.2	4.0	—	—	17.99	16.5	18.84	16.5

R_{eff} is the half light radius. q denotes the axis ratio. P.A. is with respect to the x-axis. The Sérsic index n controls the degree of curvature of the galaxy light profile. Magnitudes m are given in the ABmag system. The only difference among systems with sources the same brightness is in the source-position, which is set to produce either two or four images of the center.

^a This configuration yields 4 QSO images.

^b This configuration yields 2 QSO images.

Table 3. Lens Model Parameters

Lens Name	z	R_{Ein} (arcsec)	q	P.A. (deg)	γ'
fainter system	0.783	1.14	0.6	14.7	2.0
brighter system	0.351	1.1	0.81	113.2	2.0

R_{Ein} is the Einstein radius, according to the definition by Kormann+94. q denotes the axis ratio of the mass distribution. P.A. is anti-clockwise from the x-axis. The model deflector is a Singular Isothermal Ellipsoid ($\gamma'=2$), which is then fit using power-law models with variable γ' .

Table 4. Point Source Parameters

Lens Name	magnitude (I)	magnitude (K)	magnitude (VIS)	magnitude (H)	magnification (I)	magnification (II)	magnification (III)	magnification (IV)
fainter system ^a	24.0	24.0	24.0	24.0	2.84	3.75	6.59	2.78
fainter system ^b	24.0	24.0	24.0	24.0	2.78	2.48	—	—
brighter system ^b	21.7	21.5	22.9	21.5	1.22	6.10	—	—
brighter system ^a	21.7	21.5	22.9	21.5	6.09	8.22	6.86	7.53

Magnitudes are given in the ABmag system. The source magnitude m is given in the source plane so that the observed magnitude in the image plane is given by $m - 2.5 \log_{10} \mu$, where μ is the magnification of image (given in the table for each image).

^a This configuration yields 4 QSO images.

^b This configuration yields 2 QSO images.

labeltab:pointsource

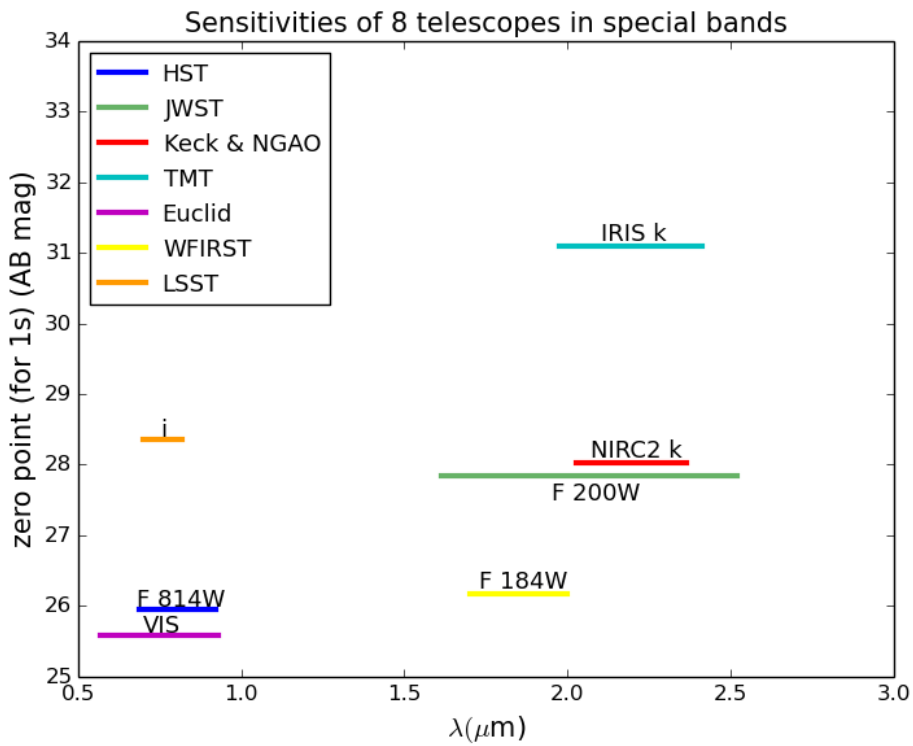


Figure 1. Zero Points in AB magnitudes of HST (blue), JWST (green), Keck & NGAO (red), TMT (cyan), Euclid (magenta), WFIRST (yellow) and LSST (orange) in units of per second. Different color bars indicate the wavelength range of each telescope used in this work.

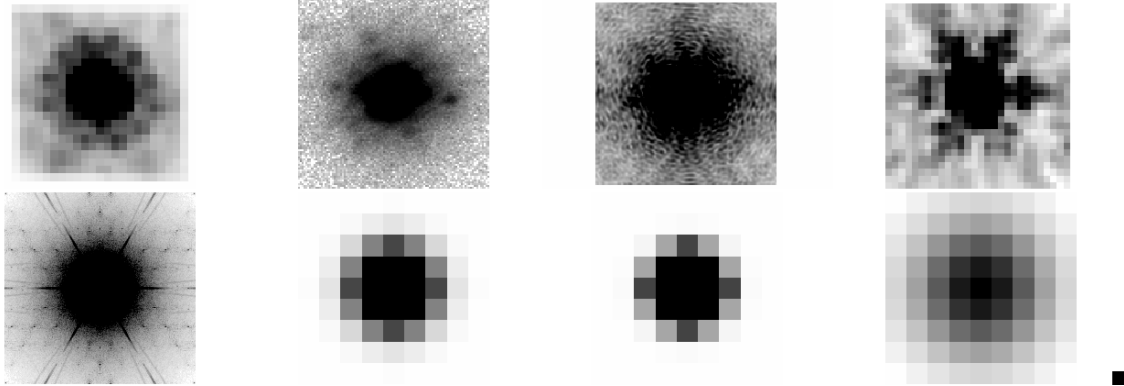


Figure 2. The typical PSF of each instrument. The upper row, from left to right, represent HST, Keck, NGAO, and JWST. The lower row, from left to right, show TMT, Euclid, WFIRST, and LSST respectively. Realistic PSFs from stars in the field are used for HST, JWST, Keck (LGSAO & NGAO), and TMT. On the other hand, the Gaussian PSFs are adopted for the other three survey instruments.

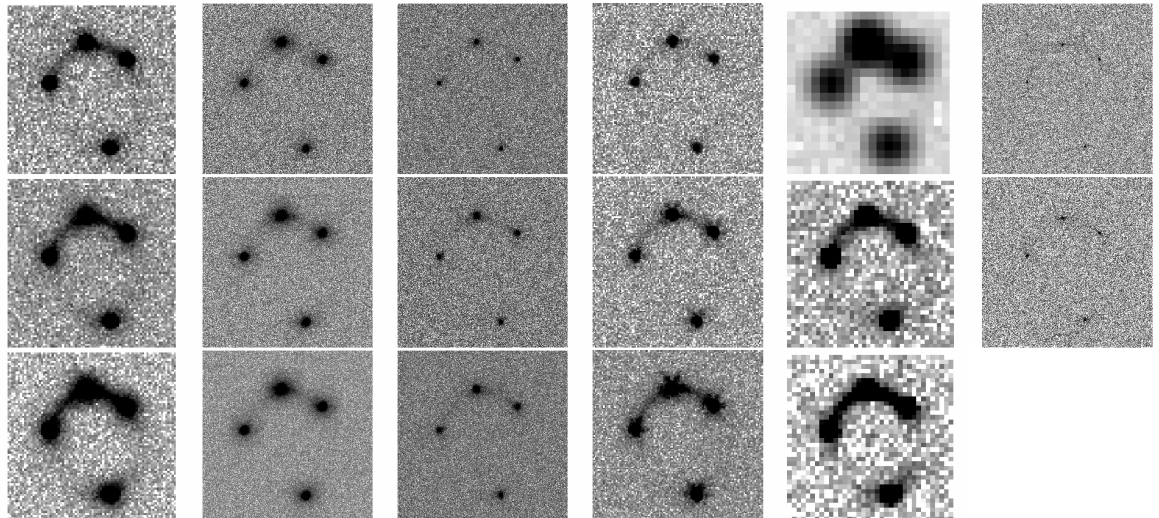


Figure 3. Simulated lens system results showing the fainter lens system (4 QSO images in the lens plane). The simulated image pixel scales are all $4'' \times 4''$. The first 4 columns, from left to right, represent HST, Keck, NGAO, and JWST; from top to bottom, correspond to $1/3 \times$ good exposure time, good exposure time, and $3 \times$ good exposure time (See the definition of “good exposure time” in Section *.*). The fifth column include 3 survey detections by 3 different telescopes, from top to bottom, for LSST, Euclid, and WFIRST respectively. The last column is for TMT with 2 fixed exposure time: 360 seconds and 1080 seconds.

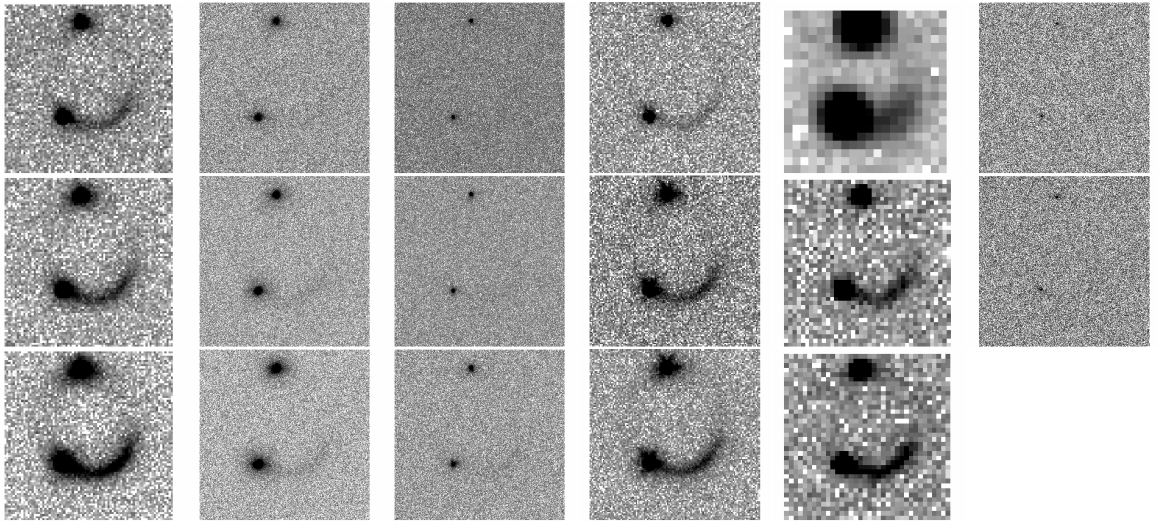


Figure 4. Same as Fig. 2, except that the simulated lens system results showing the fainter lens system (2 QSO images in the lens plane).

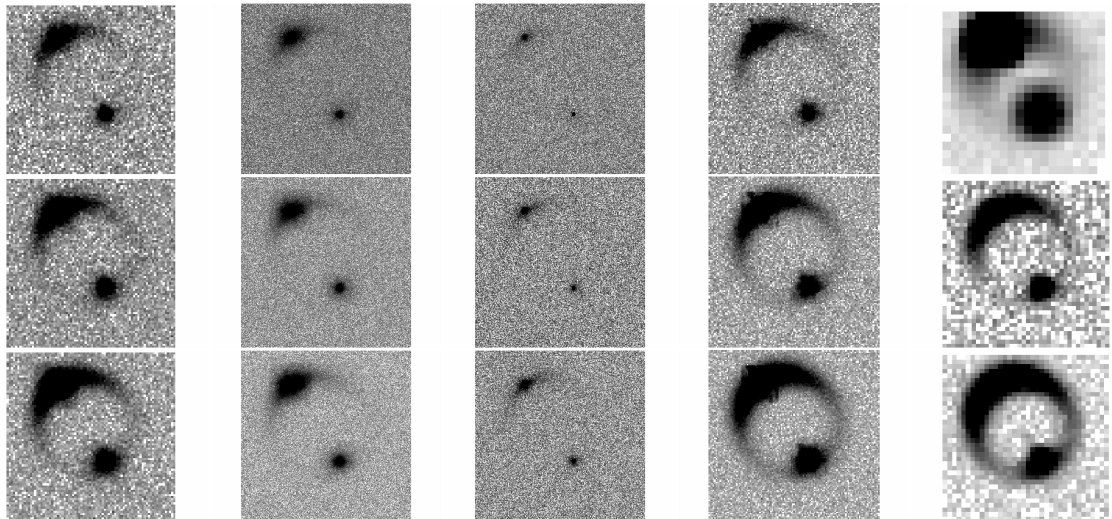


Figure 5. Simulated lens system results showing the brighter lens system (2 QSO images in the lens plane). The simulated image pixel scales are all $4'' \times 4''$. The first 3 columns, from left to right, present HST, Keck, and NGAO; from top to bottom, correspond to $1/3 \times$ good exposure time, good exposure time, and $3 \times$ good exposure time. The fourth column shows JWST with 3 fixed exposure time: 60 seconds, 180 seconds, and 540 seconds. The last column include 3 survey detections by 3 different telescopes, from top to bottom, for LSST, Euclid, and WFIRST respectively.

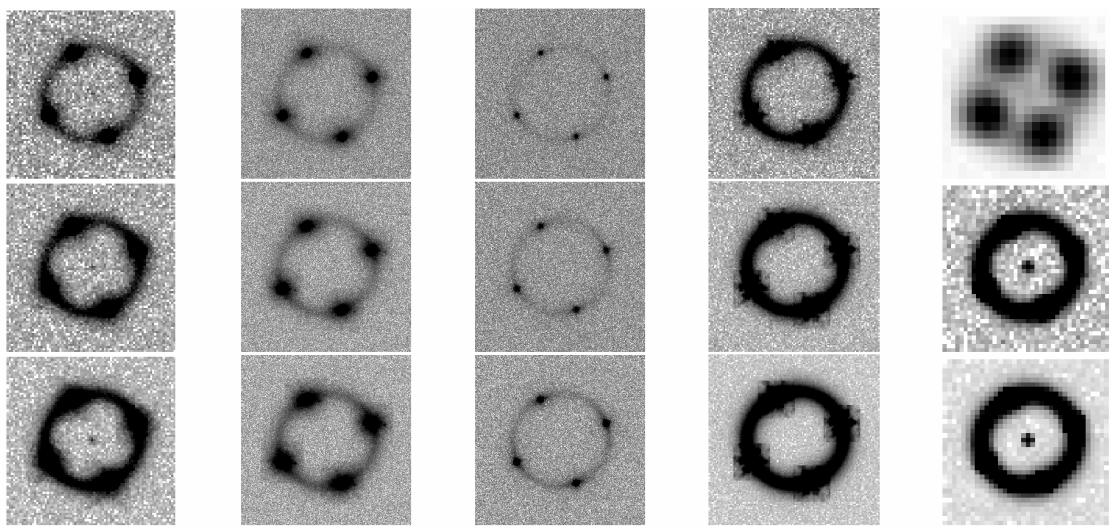


Figure 6. Same as Fig. 4, except that the simulated lens system results showing the brighter lens system (4 QSO images in the lens plane). The black spots in the center of the simulated images using HST, Euclid and WFIRST are from the efforts of strong signal pixels, so it's a “ghost” image which can be ignored.

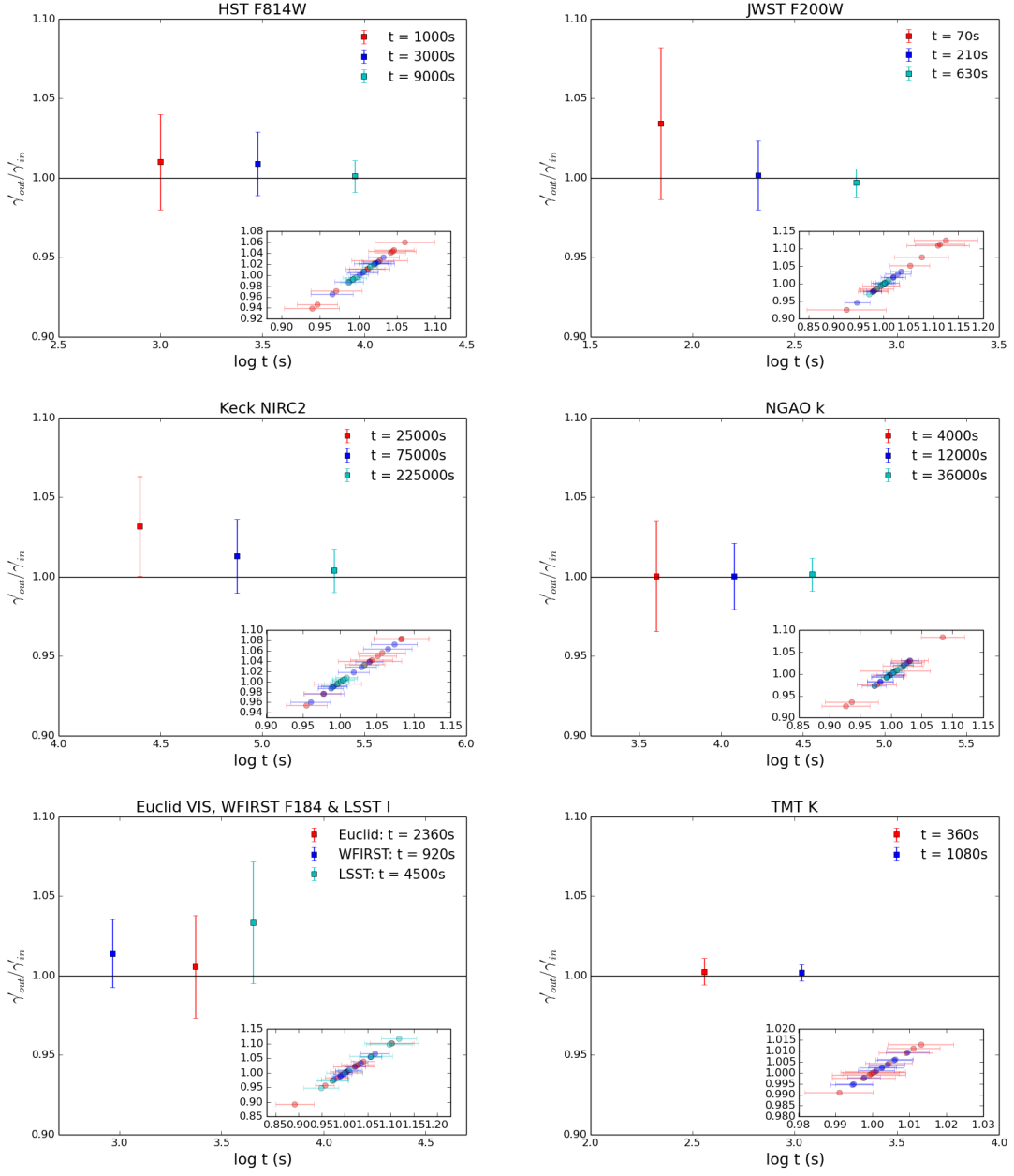


Figure 7. The ability of recovering mass slope with respect to different exposure time for a variety of telescopes. This figure shows the fainter lens system with 4 QSO images in the lens plane. γ'_{in} is the input SIE mass slope. γ'_{out} is drawn from MCMC sampling based on the simulated images given γ'_{in} . The error bar represents 1σ confidence range. The insert in each panel shows all 10 simulation results for each exposure time with the same color coding. Note that both axes represent $\gamma'_{out}/\gamma'_{in}$ whereas error bars are only shown on the x-axis for clarity.

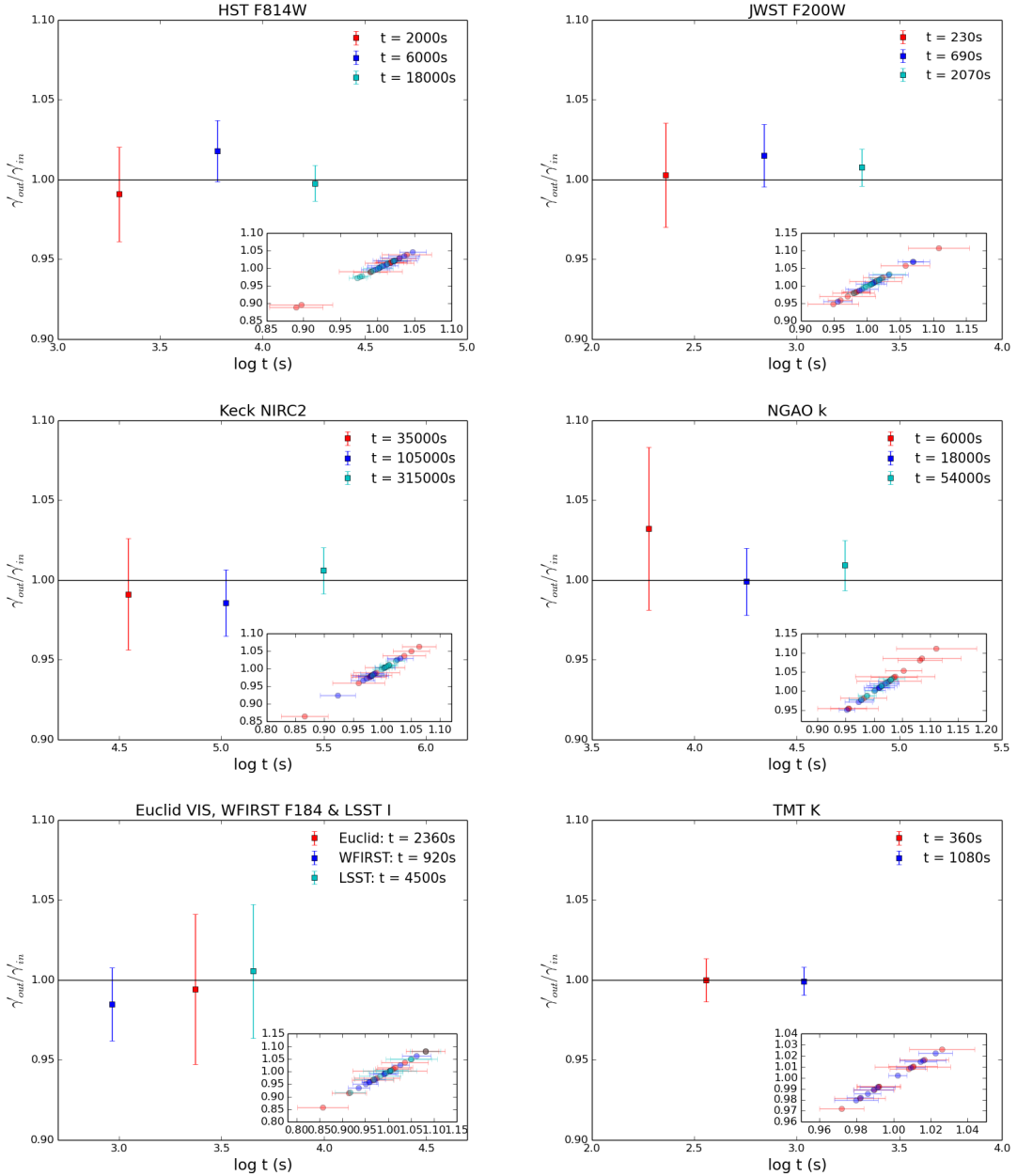


Figure 8. Same as Fig. 6, except that this figure is shown for the fainter lens system with 2 QSO images in the lens plane.

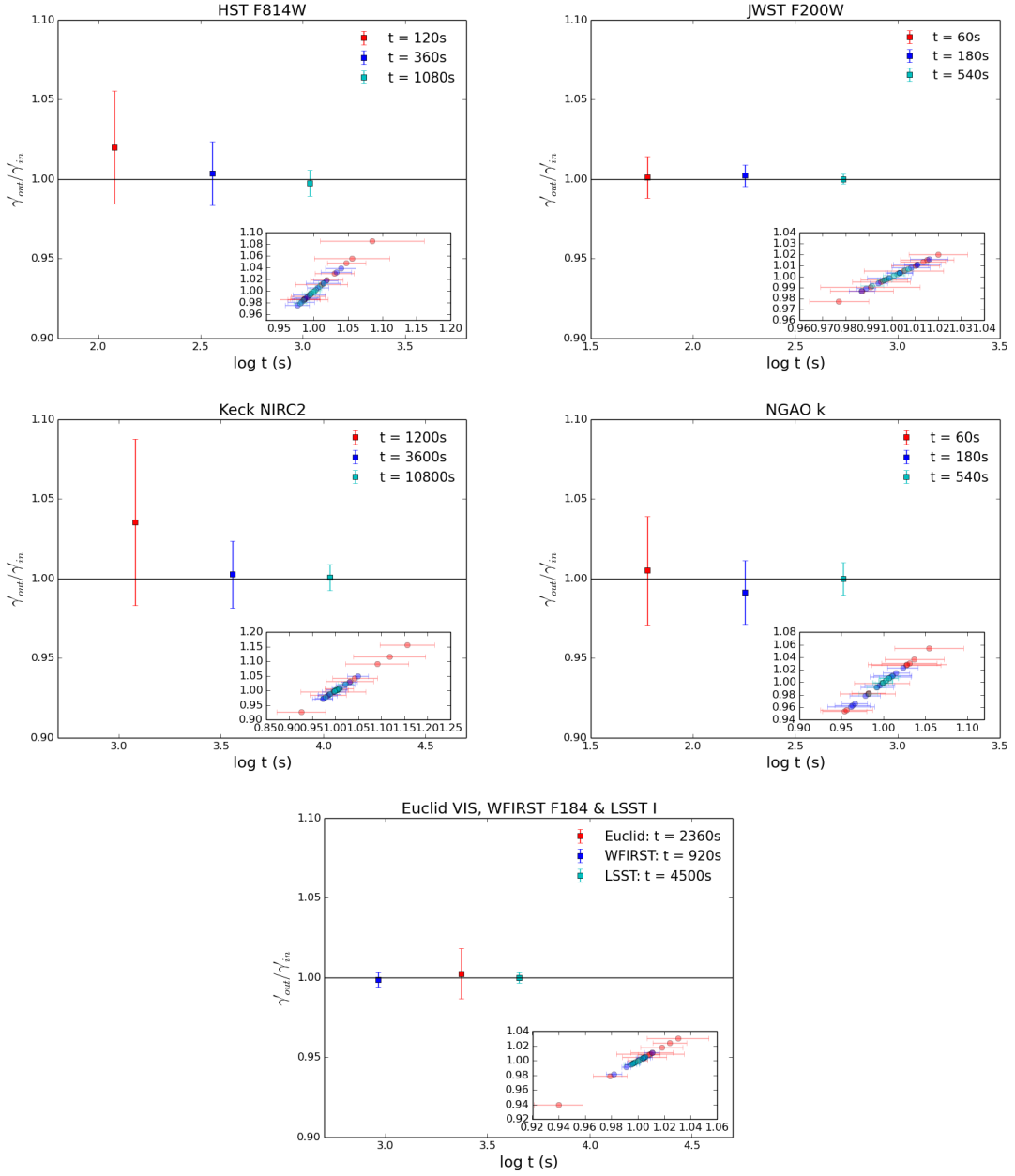


Figure 9. Same as Fig. 6, except that this figure is shown for the brighter lens system with 2 QSO images in the lens plane.

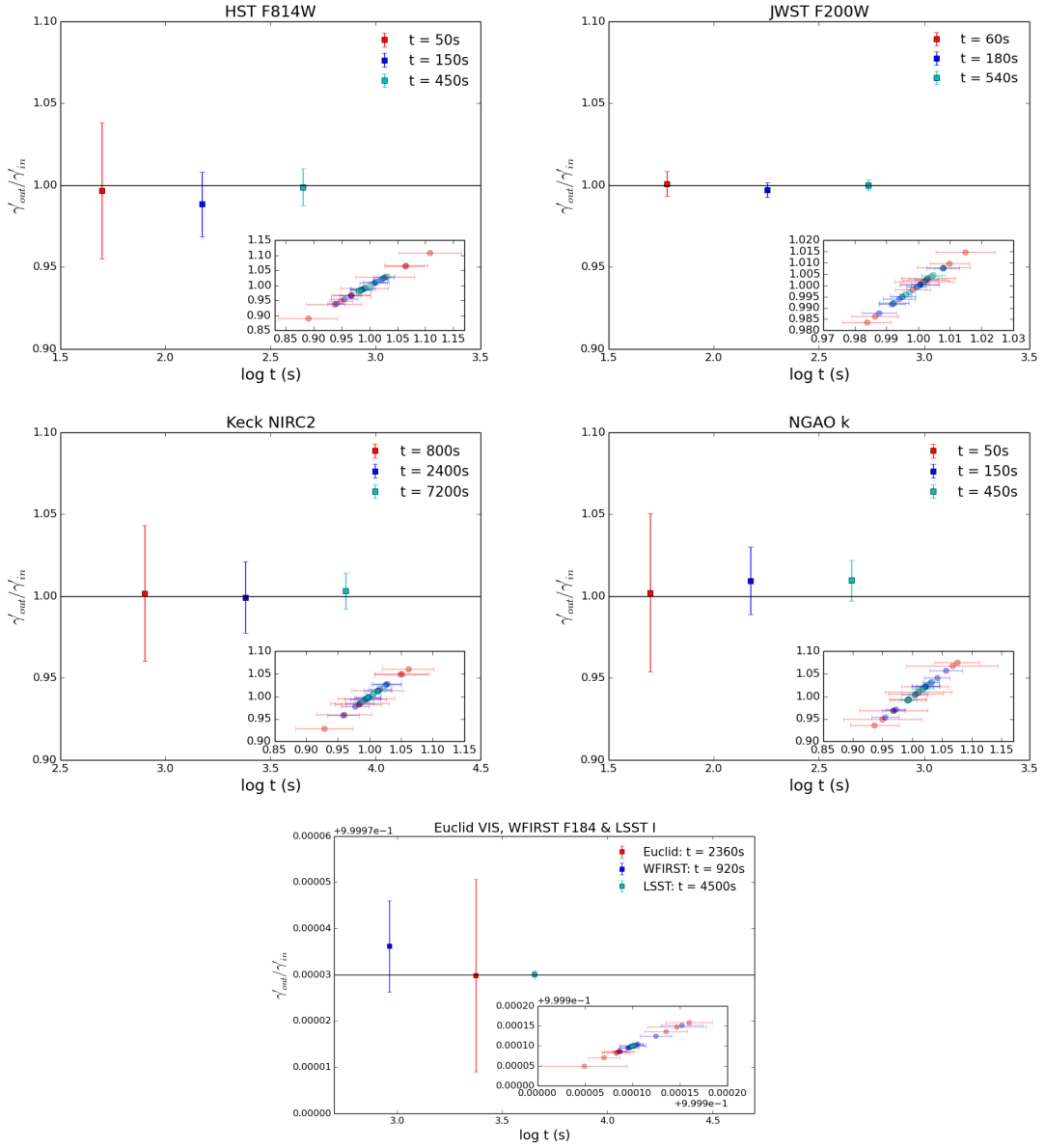


Figure 10. Same as Fig. 6, except that this figure is shown for the brighter lens system with 4 QSO images in the lens plane.